Journal of Power Sources Advances 32 (2025) 100170

Contents lists available at ScienceDirect

Journal of Power Sources Advances

journal homepage: www.sciencedirect.com/journal/journal-of-power-sources-advances

Cathode flow velocity and pressure gradient oscillations in impedance spectroscopy of PEM fuel cells

Andrei Kulikovsky

Forschungszentrum Jülich GmbH, Theory and Computation of Energy Materials (IET-3), Institute of Energy and Climate Research, D–52425 Jülich, Germany

ARTICLE INFO

Keywords:
PEMFC
Laminar flow in the channel
Permeable wall
Berman's model
Impedance spectroscopy

ABSTRACT

In electrochemical impedance spectroscopy experiments with PEM fuel cells, the applied AC current induces oscillations of the mass flow across the gas diffusion layer/cathode channel interface. These oscillations perturb the air flow velocity and pressure in the cathode channel. By analogy with Berman's approach, the transient Navier–Stokes equations for air flow in a channel with a permeable wall are reduced to a single equation for the transverse profile of the streamwise flow velocity (SFV). Linearization and Fourier-transformation of this equation leads to an ODE for the SFV perturbation amplitude. The numerical solution shows that harmonic perturbation of the cell current density generates oscillations of the pressure gradient and SFV. As the frequency increases, the transverse shape of the SFV oscillations amplitude flattens in the main body of the flow, while the peaks form at the channel walls. Averaged across the channel amplitudes of pressure gradient and SFV oscillations linearly increase along the channel. Analytical formulas for incorporation of these effects into impedance models for PEM fuel/electrolysis cell are derived.

1. Introduction

Laminar flow of incompressible fluid in a channel with permeable wall(s) is of interest for applications in ultrafiltration [1] and fuel cells [2]. In PEM fuel cells, oxygen leaves the cathode channel through the channel/gas diffusion layer (GDL) interface to participate in the oxygen reduction reaction (ORR), while a flux of water produced in the ORR enters the channel through this interface. During EIS experiments, applied AC current perturbation induces harmonic oscillations of the aforementioned oxygen and water fluxes.

In 1953, Berman [3] considered the 2D problem of a steady-state flow between parallel permeable walls with a constant velocity of mass injection. He reduced the problem to a single ODE for the transverse shape of the streamwise flow velocity (SFV) and provided an elegant asymptotic solution. Later, Berman's approach was used to solve the problem of a flow in pipes and ducts with permeable walls and a variable along the pipe/duct velocity of suction/injection [4–8]. However, non-stationary effects due to the time-dependent injection velocity have not been considered in the literature.

In 1929, Richardson and Tyler [9] reported measurements of oscillatory flow in a pipe with impermeable wall induced by a harmonic longitudinal pressure gradient. They demonstrated the formation of a velocity oscillations peak amplitude near the pipe wall. One year later, Sexl [10] developed a model for oscillatory flow in a circular pipe and derived a simple solution for the radial shape of the oscillations velocity amplitude. He showed that this amplitude is distributed along the pipe radius according to the Bessel function with a peak (shoulder) at the distance

$$l_* = \sqrt{\frac{\nu}{\omega}} \tag{1}$$

from the wall. Here ν is the kinematic viscosity of the gas and ω is the angular frequency of the perturbation. Harris, Peevt, and Wilkinson [11] made precise measurements which confirmed Sexl's result. In all these works, the velocity oscillations were induced by harmonic variation of the longitudinal pressure gradient.

Following a pioneering work by Springer et al. [12], there has been a growing interest in physics-based models for PEM fuel cell impedance over the past two decades [13–34]. One of the goals of this type of modeling is to develop fast models suitable for fitting experimental spectra [24,25,29,30,32,35–37]. The typical stoichiometry of air flow in the PEMFC cathode channel is about 2, meaning that the oxygen concentration and current density are non-uniform along the channel coordinate. Furthermore, oxygen concentration in the channel oscillates due to the applied AC signal. At low air flow stoichiometry of 2, the transport of these oscillations along the channel leads to the formation of a low-frequency arc in the cell impedance spectra [38,39]. So far, however, sub-models for the channel flow in cell impedance models employed the assumption of constant (unperturbed) flow velocity [35,40]. It is worth noting that the models for

E-mail address: A.Kulikovsky@fz-juelich.de.

https://doi.org/10.1016/j.powera.2025.100170
Received 30 November 2024; Received in revised form 23 January 2025; Accepted 28 January 2025
Available online 7 February 2025

Nomenclature

~	Marks dimensionless variables
c	Oxygen molar concentration, mol cm^{-3}
F	Faraday constant, C mol^{-1}
f	Dimensionless function, Eq. (10); frequency Hz
f_*	Characteristic frequency, Hz, Eq. (35)
j_0	Mean cell current density, A cm^{-2}
h	Channel depth, cm
$\mathfrak{I}$	Imaginary part
i	Imaginary unit
i_*	Volumetric exchange current density, A cm^{-3}
k	Constant of integration, Eq. (23)
L	Channel length, cm
l_*	Distance from the peak to the wall, Eq. (1)
M_w, M_{ox}	Water and oxygen molar masses, kg mol^{-1}
p	Pressure, Pa
R	Dimensionless parameter, Eq. (13)
Re	Reynolds number, Eq. (9)
$\mathfrak{R}$	Real part
t	Time, s
u, v	Flow velocity components, m s^{-1}
u_0	Inlet flow velocity, m s^{-1}
w	Velocity of mass suction/injection, m s^{-1}
x	Coordinate along the air channel, m
y	Coordinate through the channel depth, m
Subscripts:	
0	Steady-state value
1	Small-amplitude perturbation
Greek:	
α	Water transfer coefficient through the membrane
λ	Air flow stoichiometry
ν	Flow kinematic viscosity, m^2 s^{-1}
ρ	Air density, kg m^{-3}
ϕ	Dimensionless parameter, Eq. (37)
ψ	Dimensionless stream function, Eq. (10)
ω	Angular frequency, s^{-1}

electrochemical pressure and concentration impedance spectroscopy do take into account the cathode flow velocity oscillations induced by the applied pressure perturbation either at the channel inlet or outlet [41–43]. However, to the best of our knowledge, SFV oscillations induced by the perturbation of the mass flow injected into the cathode channel have not yet been considered in impedance modeling.

The air flow in the cathode channel of PEM fuel cells has been studied by means of numerical solution of 2D or 3D fluid dynamics equations using CFD solvers [44–48]. This method requires a sophisticated software and powerful computers and it is hardly suitable for incorporation into cell impedance models.

The Reynolds number of the flow in a fuel cell channel is typically well below 1000 and hence such flow is laminar. Laminar subsonic flow in a channel can be treated as incompressible [49]. Below, the unsteady laminar flow of an incompressible fluid between parallel walls with a time-dependent mass injection through one of the walls is considered. In analogy to Berman's approach, the system of unsteady 2d Navier–Stokes equations is reduced to a single 1d transient equation for the transversal shape of the SFV. The equation allows us to study the flow response to a small-amplitude harmonic perturbation of the mass injection velocity. The aim of the work is to answer the question of what happens to the flow in the cathode channel of a PEM fuel cell when AC current perturbations are applied in electrochemical impedance spectroscopy (EIS) experiments and how these effects can be incorporated into impedance models suitable for spectra fitting.

It is shown that the harmonic injection velocity causes longitudinal oscillations in the SFV and pressure gradient. At low frequencies, the amplitude of the SFV oscillations has a parabolic Poiseuille-like shape across the channel. As the frequency increases, this shape flattens in the main body of the flow, while two sharp peaks form at the distance given by Eq. (1) from the channel walls. The average across the channel amplitudes of the pressure gradient and the flow velocity oscillations increase linearly with the distance along the channel. To illustrate the solutions, we calculate the amplitude of the SFV oscillations induced in PEM fuel and electrolysis cells by small harmonic perturbations of the cell current typical for EIS.

2. Model

2.1. Basic equations

Consider the laminar flow of an incompressible fluid between parallel walls separated by the distance h, with the upper wall permeable to mass injection (Fig. 1). Water injected in the PEM fuel cell channel is assumed to be in the gas phase. Possible water condensation in the channel is neglected. The momentum conservation Navier–Stokes equations for the streamwise u and normal v flow velocity components are [49]

$$\frac{\partial u}{\partial t}+u\frac{\partial u}{\partial x}+v\frac{\partial u}{\partial y}=-\frac{1}{\rho}\frac{\partial p}{\partial x}+\nu\left(\frac{\partial^2 u}{\partial x^2}+\frac{\partial^2 u}{\partial y^2}\right) \tag{2}$$

$$\frac{\partial v}{\partial t}+u\frac{\partial v}{\partial x}+v\frac{\partial v}{\partial y}=-\frac{1}{\rho}\frac{\partial p}{\partial y}+\nu\left(\frac{\partial^2 v}{\partial x^2}+\frac{\partial^2 v}{\partial y^2}\right) \tag{3}$$

Here p is the pressure, ρ the flow density, and ν the flow kinematic viscosity. As ρ is constant, the continuity equation reads

$$\frac{\partial u}{\partial x}+\frac{\partial v}{\partial y}=0. \tag{4}$$

Introducing dimensionless variables

$$\tilde{t}=\frac{tu_0}{h},\quad \tilde{x}=\frac{x}{h},\quad \tilde{y}=\frac{y}{h},\quad \tilde{u}=\frac{u}{u_0},\quad \tilde{v}=\frac{v}{u_0},$$

$$\tilde{p}=\frac{p}{\rho u_0^2},\quad \tilde{\omega}=\frac{\omega h}{u_0}, \tag{5}$$

Eqs. (2)–(4) transform to

$$\frac{\partial \tilde{u}}{\partial \tilde{t}}+\tilde{u}\frac{\partial \tilde{u}}{\partial \tilde{x}}+\tilde{v}\frac{\partial \tilde{u}}{\partial \tilde{y}}=-\frac{\partial \tilde{p}}{\partial \tilde{x}}+\frac{1}{\mathrm{Re}}\left(\frac{\partial^2 \tilde{u}}{\partial \tilde{x}^2}+\frac{\partial^2 \tilde{u}}{\partial \tilde{y}^2}\right) \tag{6}$$

$$\frac{\partial \tilde{v}}{\partial \tilde{t}}+\tilde{u}\frac{\partial \tilde{v}}{\partial \tilde{x}}+\tilde{v}\frac{\partial \tilde{v}}{\partial \tilde{y}}=-\frac{\partial \tilde{p}}{\partial \tilde{y}}+\frac{1}{\mathrm{Re}}\left(\frac{\partial^2 \tilde{v}}{\partial \tilde{x}^2}+\frac{\partial^2 \tilde{v}}{\partial \tilde{y}^2}\right) \tag{7}$$

$$\frac{\partial \tilde{u}}{\partial \tilde{x}}+\frac{\partial \tilde{v}}{\partial \tilde{y}}=0, \tag{8}$$

where

$$\mathrm{Re}=\frac{u_0 h}{\nu} \tag{9}$$

is the inlet Reynolds number, u_0 the mean over the y–axis streamwise component of inlet flow velocity, and h the channel depth.

In analogy to Berman's work [3], we introduce a stream function

$$\psi=\left(1+\int_0^{\tilde{x}}\tilde{w}\left(\tilde{t},\xi\right)\,d\xi\right)f\left(\tilde{t},\tilde{y}\right) \tag{10}$$

where $\tilde{w}$ is the dimensionless velocity of injection. Setting

$$\tilde{u}=\frac{\partial \psi}{\partial \tilde{y}},\quad \tilde{v}=-\frac{\partial \psi}{\partial \tilde{x}}, \tag{11}$$

Eq. (4) is satisfied. For $\tilde{u}$ and $\tilde{v}$ we thus have

$$\tilde{u}=(1+R)f',\quad \tilde{v}=-\tilde{w}f \tag{12}$$

where

$$R\equiv\int_0^{\tilde{x}}\tilde{w}\left(\tilde{t},\xi\right)\,d\xi \tag{13}$$

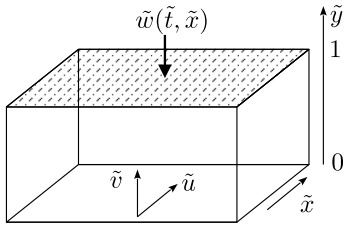

Fig. 1. Schematic of the channel. The hatched area indicates the permeable wall through which the mass enters or leaves the channel.

and the prime sign denotes the partial derivatives of f over $\tilde{y}$ and $\tilde{w}$ over $\tilde{x}$:

$$f' \equiv \frac{\partial f}{\partial \tilde{y}}, \quad \tilde{w}' \equiv \frac{\partial \tilde{w}}{\partial \tilde{x}}. \tag{14}$$

Note that, strictly speaking, f in Eq. (10) is also a function of $\tilde{x}$, and the exact expression for $\tilde{v}$ in Eq. (12) is

$$\tilde{v} = -\tilde{w}f - (1+R)\frac{\partial f}{\partial \tilde{x}} \tag{15}$$

However, under conditions typical of the problems discussed, R and the derivative $\partial f/\partial \tilde{x}$ are small. An estimate shows that the second term in Eq. (15) is four orders of magnitude smaller than the first one (Appendix), and it can be safely neglected.

Substituting Eqs. (12) into Eqs. (6), (7) we come to

$$\frac{\partial(1+R)f'}{\partial \tilde{t}} + (1+R)\tilde{w}\left(f'f' - ff''\right) = -\frac{\partial \tilde{p}}{\partial \tilde{x}} + \frac{1}{\mathrm{Re}}\left(\tilde{w}'f' + (1+R)f'''\right) \tag{16}$$

$$-\frac{\partial(\tilde{w}f)}{\partial \tilde{t}} + \left(\tilde{w}^2 - (1+R)\tilde{w}'\right)ff' = -\frac{\partial \tilde{p}}{\partial \tilde{y}} - \frac{1}{\mathrm{Re}}\left(\tilde{w}''f + \tilde{w}f''\right) \tag{17}$$

Differentiating Eq. (16) over $\tilde{y}$ and Eq. (17) over $\tilde{x}$ we arrive at

$$\frac{\partial(1+R)f''}{\partial \tilde{t}} + (1+R)\tilde{w}\left(f'f'' - ff'''\right) = -\frac{\partial}{\partial \tilde{y}}\left(\frac{\partial \tilde{p}}{\partial \tilde{x}}\right) + \frac{1}{\mathrm{Re}}\left(\tilde{w}'f'' + (1+R)f''''\right) \tag{18}$$

$$-\frac{\partial(\tilde{w}'f)}{\partial \tilde{t}} + \left(\tilde{w}\tilde{w}' - (1+R)\tilde{w}''\right)ff' = -\frac{\partial}{\partial \tilde{x}}\left(\frac{\partial \tilde{p}}{\partial \tilde{y}}\right) - \frac{1}{\mathrm{Re}}\left(\tilde{w}'''f + \tilde{w}'f''\right) \tag{19}$$

Subtracting Eq. (19) from Eq. (18) the terms with pressure gradient cancel out and we come to

$$\frac{\partial}{\partial \tilde{t}}\left((1+R)f'' + \tilde{w}'f\right) + (1+R)\tilde{w}\left(f'f'' - ff'''\right) - \left(\tilde{w}\tilde{w}' - (1+R)\tilde{w}''\right)ff' = \frac{1}{\mathrm{Re}}\left(2\tilde{w}'f'' + (1+R)f'''' + \tilde{w}'''f\right) \tag{20}$$

Eq. (20) is the general equation for the problem of a flow in a channel with a non-uniform along $\tilde{x}$, time-dependent velocity of mass injection. The boundary conditions for Eq. (20) follow from Eqs. (12) and the no-slip condition at the walls

$$f(1) = 1, \quad f'(1) = 0, \quad f(0) = f'(0) = 0 \tag{21}$$

Here, $f(1) = 1$, follows from the second of Eqs. (12), the zero derivatives $f'(0) = f'(1) = 0$ mean the no-slip conditions, and zero $f(0) = 0$ means the impermeable wall at $\tilde{y} = 0$.

2.2. Small-amplitude oscillations of a uniform along $\tilde{x}$ injection velocity

Below, we consider a simpler case of uniform along $\tilde{x}$ injection velocity $\tilde{w}(\tilde{t})$. Setting in Eq. (20) $R = \tilde{w}\tilde{x}$ and chalking out the terms with $\tilde{w}'$, $\tilde{w}''$, and $\tilde{w}'''$, we arrive at

$$\left(\frac{\tilde{x}}{1+\tilde{x}\tilde{w}}\right)\frac{\partial \tilde{w}}{\partial \tilde{t}}f'' + \frac{\partial f''}{\partial \tilde{t}} + \tilde{w}\left(f'f'' - ff'''\right) = \frac{f''''}{\mathrm{Re}}. \tag{22}$$

Eq. (22) can be integrated over $\tilde{y}$ once, leading to

$$\left(\frac{\tilde{x}}{1+\tilde{x}\tilde{w}}\right)\frac{\partial \tilde{w}}{\partial \tilde{t}}f' + \frac{\partial f'}{\partial \tilde{t}} + \tilde{w}\left(f'f' - ff''\right) - \frac{f'''}{\mathrm{Re}} = k, \tag{23}$$

where k is the constant parameter determined from solution of Eq. (23) with the four boundary conditions, Eq. (21). Eq. (23) is the non-stationary extension of the steady-state Eq. (24) derived by Berman [3]:

$$\tilde{w}\left(f'f' - ff''\right) - \frac{f'''}{\mathrm{Re}} = k. \tag{24}$$

Indeed, Eq. (24) is obtained by chalking out the terms with time derivatives in Eq. (23). Note that the transient term in Eq. (23) parametrically depends on $\tilde{x}$.

Below, the subscripts 0 and 1 mark the static variables and the small-amplitude perturbations, respectively. Substituting

$$\begin{aligned} &\tilde{w}(\tilde{t}) = \tilde{w}_0 + \tilde{w}_1(\tilde{\omega})\exp(\mathrm{i}\tilde{\omega}\tilde{t}), \quad |\tilde{w}_1| \ll |\tilde{w}_0| \\ &f(\tilde{y},\tilde{t}) = f_0(\tilde{y}) + f_1(\tilde{\omega},\tilde{y})\exp(\mathrm{i}\tilde{\omega}\tilde{t}), \quad |f_1| \ll |f_0| \\ &k = k_0 + k_1 \end{aligned} \tag{25}$$

into Eq. (23), neglecting terms with the perturbation product and subtracting the static Eq. (24), we come to a linear problem for the complex perturbation amplitude $f_1(\tilde{\omega},\tilde{y})$:

$$\mathrm{i}\tilde{\omega}\left(\frac{\tilde{x}\tilde{w}_1 f_0'}{1+\tilde{x}\tilde{w}_0} + f_1'\right) + \tilde{w}_0\left(f_0(2f_1' - f_1'') - f_0''f_1\right) + \tilde{w}_1\left(f_0'f_0' - f_0f_0''\right) - \frac{f_1'''}{\mathrm{Re}} = k_1 \tag{26}$$

where $f_0(\tilde{y})$ obeys to the static Berman's equation Eq. (24). Eq. (26) describes the SFV response to the small-amplitude perturbation of the injection velocity $\tilde{w}_1$ caused by the applied potential or current perturbation in EIS experiments.

Eq. (26) is an ODE for the function $f_1(\tilde{y})$ with $\tilde{x}$ and $\tilde{\omega}$ being the varying parameters. The parameter k_1 is constant; if necessary, k_1 could be eliminated by differentiating Eq. (26) over $\tilde{y}$. The boundary condition for f_1 at $\tilde{y} = 1$ (permeable upper wall, Fig. 1) follows from equation $\tilde{v}_0 + \tilde{v}_1 = -(\tilde{w}_0 + \tilde{w}_1)(f_0 + f_1)$. Neglecting the product $\tilde{w}_1 f_1$ and considering that $\tilde{v}_0 = -\tilde{w}_0 f_0$, $f_0(1) = 1$, and $\tilde{v}_1 = -\tilde{w}_1$ we get $f_1(1) = 0$. Thus, the boundary conditions for Eq. (26) are

$$f_1(1) = f_1'(1) = f_1(0) = f_1'(0) = 0. \tag{27}$$

2.3. Perturbation amplitude of the pressure gradient

The 2d shape of longitudinal pressure gradient is given by Eq. (16). Chalking out the term with $\tilde{w}'$, for the $\tilde{y}$–profile of the pressure gradient $\partial\tilde{p}/\partial\tilde{x}$ we get

$$-\frac{\partial \tilde{p}}{\partial \tilde{x}} = \frac{\partial(1+R)f'}{\partial \tilde{t}} + (1+R)\tilde{w}\left(f'f' - ff''\right) - \frac{1}{\mathrm{Re}}(1+R)f''' \tag{28}$$

Substituting here Eqs. (25) and

$$\tilde{p} = \tilde{p}_0(\tilde{y};\tilde{x}) + \tilde{p}_1(\tilde{\omega},\tilde{y};\tilde{x})\exp(\mathrm{i}\tilde{\omega}\tilde{t}), \quad |\tilde{p}_1| \ll |\tilde{p}_0| \tag{29}$$

and subtracting the static equation for $\tilde{p}_0$ we come to the linear equation for the gradient of a small pressure perturbation amplitude

$$-\frac{\partial \tilde{p}_1}{\partial \tilde{x}} = \mathrm{i}\tilde{\omega}\left(\tilde{w}_1\tilde{x}f_0 + (1+\tilde{w}_0\tilde{x})f_1'\right) + \tilde{w}_1\left(1+2\tilde{w}_0\tilde{x}\right)\left(f_0'f_0' - f_0f_0''\right) + \tilde{w}_0(1+\tilde{w}_0\tilde{x})\left(2f_0'f_1' - f_0f_1'' - f_1f_0''\right) - \frac{1}{\mathrm{Re}}\left((1+\tilde{w}_0\tilde{x})f_1''' + \tilde{w}_1\tilde{x}f_0'''\right) \tag{30}$$

where the terms with the perturbation product were neglected. The first term on the right side of Eq. (30) is proportional to $\mathrm{i}\tilde{\omega}$, which shows that $\partial\tilde{p}_1/\partial\tilde{x}$ oscillates. This makes the problem qualitatively similar (but not equivalent) to the problem considered by Sexl [10].

3. Results and discussion

The numerical solutions of Eqs. (24) and (26) discussed below are derived using the standard Python BVP solver *solve_bvp*. This simplicity is a major advantage of the Berman approach used here.

3.1. Flow in the cathode channel of a PEM fuel cell

This section demonstrates the main features of the solution to Eqs. (24) and (26) for PEM fuel cells. The cell parameters used in the calculations are listed in Table 1. The amplitude of the applied AC current perturbation is typical for EIS measurements with PEMFCs [50], hence the example below shows what happens to the cathode channel flow during EIS measurements.

The mass flux injected into the cathode channel through the channel/GDL interface is

$$\rho w_0 = \frac{\big(2(1+2\alpha)M_w - M_{ox}\big)j_0}{4F} \tag{31}$$

where ρ is the density of air, M_w and M_{ox} are the molecular weights of water and oxygen, respectively, α is the net water transfer coefficient from the anode to the cathode, and j_0 is the local current density. For simplicity, j_0 and α are assumed to be constant along the channel. The dimensionless steady-state injection velocity is thus

$$\tilde{w}_0 = \frac{\big(2(1+2\alpha)M_w - M_{ox}\big)j_0}{4F\rho u_0} \tag{32}$$

The amplitude of the streamwise flow velocity oscillations $\tilde{u}_1$ is determined from Eq. (12). We write

$$\begin{aligned}\tilde{u} &= \tilde{u}_0 + \tilde{u}_1 = (1+R_0+R_1)(f_0' + f_1') \\ &\simeq (1+R_0)f_0' + R_1 f_0' + (1+R_0)f_1'\end{aligned} \tag{33}$$

where the perturbation product $R_1 f_1'$ is neglected. The first term on the right side is the static flow velocity $\tilde{u}_0$, and hence $\tilde{u}_1$ is given by

$$\tilde{u}_1 = R_1 f_0' + (1+R_0)f_1' = i\tilde{w}_1\tilde{x}f_0' + (1+i\tilde{w}_0\tilde{x})f_1' \tag{34}$$

Note the frequency-independent term $i\tilde{w}_1\tilde{x}f_0'$ in Eq. (34), which is proportional to the perturbation amplitude $i\tilde{w}_1$ of the injection velocity.

The Nyquist spectrum of u_1 at the mid-plane $\tilde{y} = 1/2$ and $\tilde{x} = 1000$ (channel outlet) obtained numerically from Eqs. (26), (24) for the parameters in Table 1 is shown in Fig. 2a. The spectrum resembles the Warburg finite-length transport impedance [51]. The characteristic frequency of the spectrum is about $f_* \simeq 200$ Hz (the peak of $-\Im(u_1)$ in Fig. 2b). Numerical calculations show that in the vicinity of half-plane $\tilde{y} = 1/2$, the frequency f_* is well described by the approximate formula

$$f_* \simeq \frac{11.5\nu}{h^2}, \tag{35}$$

i.e., f_* is determined by the viscous friction at the channel walls and by the channel depth. Closer to the walls, the numerical coefficient in Eq. (35) grows rapidly; however, the parametric dependence $f_* \sim \nu/h^2$ remains the same.

Of particular interest is the shape of the real part $\Re(u_1)$ which represents the SFV oscillations in phase with the applied perturbation. The $\tilde{y}$–shapes of u_1 at $\tilde{x} = 1000$ (channel outlet) for the three frequencies is shown in Fig. 3. Up to $f \simeq 1$ Hz, the $\tilde{y}$–shape of $\Re(\tilde{u}_1)$ is indistinguishable from the parabolic Poiseuille profile. However, with increasing frequency, two "shoulders" form at the walls, as predicted by Sexl [10] (Fig. 3). With further frequency increase, every shoulder moves toward the wall, while the curve between the shoulders flattens (solid line in Fig. 3), meaning that the bulk volume of the flow oscillates with the same amplitude. The curves in Fig. 3 are nearly symmetrical with respect to the half-plane $\tilde{y} = 1/2$ due to smallness of the static injection velocity w_0.

The position of the shoulders in Fig. 3 can be calculated by considering the simpler problem of flow with zero $w_0 = 0$ and non-zero $w_1 > 0$. In other words, consider the flow at zero static injection velocity, which is periodically perturbed by the small-amplitude AC injection velocity w_1 (excited Poiseuille flow). An equation for the flow velocity spectrum is obtained by setting $\tilde{w}_0 = 0$ in Eq. (26). Furthermore, at large frequencies, the frequency independent term $i\tilde{w}_1\big(f_0'f_0' - f_0 f_0''\big)$ in

Table 1
The cell parameters for the calculations of flow velocity oscillations in PEMFC cathode channel.

Cell temperature, K	273 + 80
Cathode absolute pressure, Pa	$1.5 \cdot 10^5$
Relative humidity RH, %	50
Air flow stoichiometry λ	2
Channel depth h, m	$0.1 \cdot 10^{-2}$
Channel length L, m	1.0
Inlet air flow velocity u_0, m s^{-1}	5.72
Velocity of mass injection w_0, m s^{-1}	$4.50 \cdot 10^{-4}$
Injection velocity perturbation amplitude w_1, m s^{-1}	$0.04 \cdot w_0$
Reynolds number Re	303
Cell current density j_0, A m^{-2}	10^4
AC amplitude of current density, A m^{-2}	400
Net water transfer coefficient through the membrane α	0.2
Air density, ρ, kg m^{-3}	1.06
Air kinematic viscosity, ν, m^2 s^{-1}	$1.886 \cdot 10^{-5}$

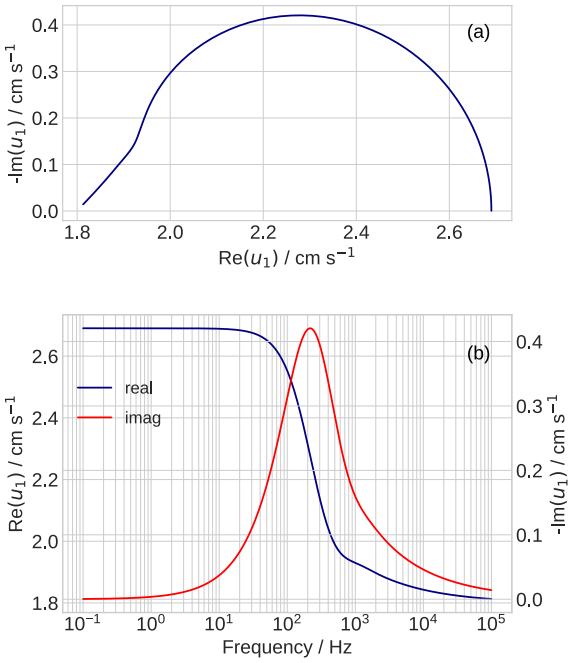

Fig. 2. (a) The Nyquist spectrum of the streamwise flow velocity oscillations amplitude u_1 at the mid-plane $\tilde{y} = 1/2$ and $\tilde{x} = 1000$ (channel outlet). (b) The frequency dependence of the real and imaginary parts of the velocity spectrum in (a).

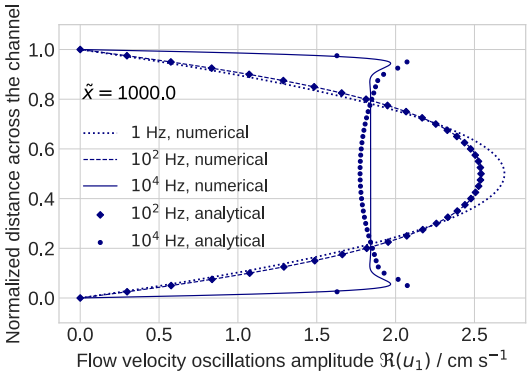

Fig. 3. Transverse shape of the SFV oscillations amplitude for the indicated frequencies at $\tilde{x} = 1000$ (channel outlet). Diamonds and dots — the analytical solution, Eq. (37), for $f = 10^2$ Hz and $f = 10^4$ Hz, respectively.

Eq. (26) can be neglected, and this equation simplifies to

$$\mathrm{i}\tilde{\omega}\left(\tilde{x}\tilde{w}_1 f_0' + f_1'\right) - \frac{f_1'''}{\mathrm{Re}} = k_1 \tag{36}$$

For the classical Poiseuille flow, $f_0' = 6\tilde{y}(1-\tilde{y})$ and the solution to Eq. (36) with the boundary conditions (27) leads to

$$f_1' = \left(\frac{\left(\sinh(\phi\,\tilde{y}) + \sinh(\phi\,(1-\tilde{y})) - \sinh(\phi)\right)\phi}{2\left(\cosh(\phi)-1\right) - \phi\sinh(\phi)} - 6\tilde{y}(1-\tilde{y}) \right) \tilde{x}\tilde{w}_1,$$
$$\phi \equiv \sqrt{\mathrm{i}\tilde{\omega}\mathrm{Re}} \tag{37}$$

Eq. (37) explicitly shows the linear dependence of f_1' on $\tilde{x}$. The diamonds and dots in Fig. 3 indicate the transverse shapes of the streamwise velocity oscillations amplitude u_1 at the channel outlet calculated from Eq. (34) with f_1' from Eq. (37). As can be seen, the analytical Eq. (37) describes the numerical result quite well.

The analytical curve for $f = 10^4$ Hz in Fig. 3 quite accurately captures the numerical peaks position. The terms with $\sinh(\phi\,\tilde{y})$ and $\sinh(\phi\,(1-\tilde{y}))$ in Eq. (37) determine peaks of the perturbation amplitude located at the distance $\tilde{l}_* \simeq 1/|\phi| = 1/\sqrt{\tilde{\omega}\mathrm{Re}}$ from the wall. In dimensional form, l_* is the distance between the peak and the wall, Eq. (1). It is worth noting that the peaks in Fig. 3 grow with $\tilde{x}$ as long as $\tilde{x}\tilde{w}_0$ is small, as shown in Eq. (26). In long channels, at $\tilde{x}\tilde{w}_0 \gg 1$ the dependence of Eq. (26) on $\tilde{x}$ disappears and the peak amplitude saturates. However, this dependence remains in the general case of a variable with $\tilde{x}$ injection velocity.

Integration of Eq. (37) over $\tilde{y} \in [0,1]$ gives

$$\langle f_1' \rangle = 0 \tag{38}$$

and since $\int_0^1 f_0'\,d\tilde{y} = \int_0^1 6\tilde{y}(1-\tilde{y})\,d\tilde{y} = 1$, for the average across the channel SFV oscillations amplitude $\langle \tilde{u}_1 \rangle$, from Eq. (34) we get

$$\langle \tilde{u}_1 \rangle \simeq \tilde{x}\tilde{w}_1 \tag{39}$$

The mean $\langle \tilde{u}_1 \rangle$ is independent of the frequency and it grows linearly along the channel coordinate $\tilde{x}$. Calculations show that Eq. (39) describes the numerical result very well.

Fig. 4 shows average over the $\tilde{y}$-coordinate negative perturbation amplitude of the pressure gradient $\Re\langle -\partial p_1/\partial\tilde{x}\rangle$, obtained numerically by integration of Eq. (30) over $\tilde{y}$. Due to the mass injection, the amplitude of the pressure gradient oscillations increases linearly along $\tilde{x}$. This growth is a key difference of the problem considered here from the one reported by Sexl [10], where the amplitude of pressure gradient oscillations does not change along $\tilde{x}$. Furthermore, the slope of $\Re\langle -\partial p_1/\partial\tilde{x}\rangle$ growth along $\tilde{x}$ increases with the frequency (Fig. 4).

An approximate analytical formula for the mean over $\tilde{y}$ amplitude of oscillating pressure gradient $\langle -\partial p_1/\partial\tilde{x}\rangle$ can be derived as follows. Substituting into Eq. (30) the solution to Eq. (36), the Poiseuille flow solution $f_0 = 3\tilde{y}^2 - 2\tilde{y}^3$, and $i\tilde{w}_0 = 0$ and integrating Eq. (30) over $\tilde{y} \in [0,1]$ yields the linear in $\tilde{x}$ function

$$\left\langle -\frac{\partial\tilde{p}_1}{\partial\tilde{x}} \right\rangle = \left(\frac{12}{5} + \frac{\tilde{\omega}N_*}{D_*}\tilde{x} \right) i\tilde{w}_1 \tag{40}$$

(Fig. 4, dots), where

$$N_* = \mathrm{i}\sqrt{2\tilde{\omega}\mathrm{Re}}(1+\cosh\phi)/2 + (1+\mathrm{i})\sinh\phi$$
$$D_* = \sqrt{2\tilde{\omega}\mathrm{Re}}(1+\cosh\phi) - 2(1-\mathrm{i})\sinh\phi \tag{41}$$

and $\phi = \sqrt{\mathrm{i}\tilde{\omega}\mathrm{Re}}$. Note that the factors N_* and D_* do not contain $i\tilde{w}_1$, hence $\langle -\partial\tilde{p}_1/\partial\tilde{x}\rangle$ is strictly proportional to the injection velocity oscillations amplitude $i\tilde{w}_1$, Eq. (40).

3.2. Flow in the water/oxygen channel of a PEM electrolysis cell

In a PEM electrolysis cell, the anode channel transports liquid water and oxygen bubbles generated in the oxygen evolution reaction. Calculation parameters for PEMEC are listed in Table 2. Application of AC current perturbation with the amplitude of 10% of the cell current density leads to the flow velocity oscillations amplitude shown in Fig. 5.

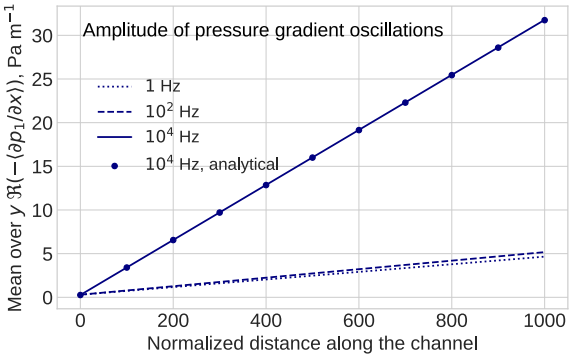

Fig. 4. Mean over $\tilde{y}$-coordinate perturbation amplitude of the pressure gradient $-\langle\Re\left(\partial p_1/\partial\tilde{x}\right)\rangle$, i.e., Eq. (30) averaged over $\tilde{y}$-coordinate. Points – approximate analytical solution, Eq. (40).

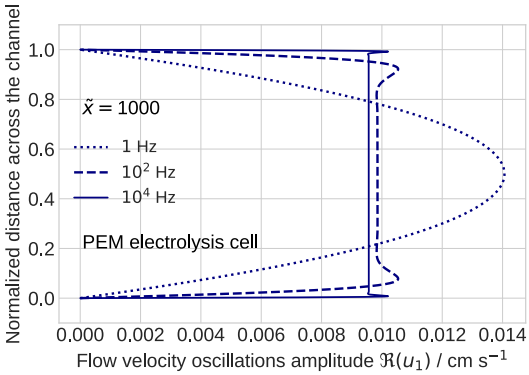

Fig. 5. Transverse shape of the amplitude of the SFV oscillations for the indicated frequencies at $\tilde{x} = 1000$ (channel outlet).

Table 2
The cell parameters for the calculations of flow velocity oscillations in PEM electrolysis cell channel.

Water flow stoichiometry λ	100
Inlet flow velocity u_0, m s^{-1}	$4.66 \cdot 10^{-2}$
Velocity of mass injection w_0, m s^{-1}	$9.53 \cdot 10^{-7}$
Reynolds number Re	128
Cell current density j_0, A m^{-2}	10^4
AC amplitude of current density, A m^{-2}	10^3
Water/oxygen volume ratio in the flow	0.5
Water kinematic viscosity, ν, m^2 s^{-1}	$3.64 \cdot 10^{-7}$

As can be seen, due to the large flow density, this amplitude is about 0.01 cm s^{-1}, much smaller than in the PEM fuel cell cathode. The feature of the perturbed water/oxygen flow is almost flat $\tilde{y}$-shape of the oscillations amplitude already at the AC frequency of 100 Hz (Fig. 5).

3.3. Concluding remarks

Growing with the distance amplitude of the cathode flow velocity oscillations so far has not been considered in PEMFC impedance modeling. In EIS experiments, the perturbation of the mass injection velocity is small. Nevertheless, this small value produces linearly growing along the channel pressure gradient, which, in turn, generates growing amplitude of the SFV oscillations, Eq. (39). In long channels, the effect can be quite significant to change the impedance.

The amplitude of the SFV oscillations increases with the cell current and with the water transfer coefficient α across the membrane. For example, if all of the water produced in the ORR and entering from the anode side would be transported into the cathode channel ($\alpha = 1$),

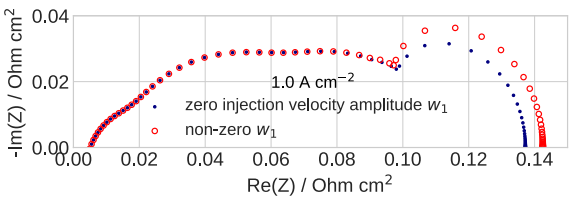

Fig. 6. The effect of the injection velocity oscillations on the PEMFC spectrum. To emphasize the effect, the net water transfer coefficient is $\alpha_w = 0.5$. The cathode catalyst layer oxygen diffusivity is $D_{ox} = 0.8 \cdot 10^{-3}$ cm^2 s^{-1}, the GDL oxygen diffusivity $D_b = 0.02$ cm^2 s^{-1}, the ORR Tafel slope $b = 0.03$ V per exponential basis, the double layer capacitance $C_{dl} = 20$ F cm^{-3}, the cable inductance is 1 nH and the cell active area is 100 cm^{-2}. All the other parameters are listed in Table 1.

the amplitude of velocity/stoichiometry oscillations would increase by a factor of five.

Comparison of the analytical and numerical solutions given above shows that the contribution of the steady-state injection velocity w_0 to the SFV and pressure gradient oscillations amplitude can be neglected (Figs. 3–4). What matters is the amplitude w_1 of the injection velocity oscillations, which is proportional to the amplitude of the applied AC current. The simple analytical solution for f_1', Eq. (37), and Eqs. (39), (40) resulting from Eq. (37) could therefore be used in PEMFC/PEMEC impedance models.

Fig. 6 illustrates the effect of the injection velocity oscillations on the PEMFC impedance spectrum. The spectra were calculated using the model [32], which takes into account the transport of oxygen perturbations along the cathode channel. Parameters for the calculation are listed in the caption to Fig. 6 and in Table 1. As can be seen, the oscillations of flow velocity increase the size of the low-frequency "channel" transport arc. Qualitatively, the effect is similar to reduction of the air flow stoichiometry.

To date, there are no measurements of pressure/velocity oscillations in the PEMFC cathode channel during EIS testing. Direct comparison of the model with an experiment is thus not possible. Calculation of the cell impedance using the corrections obtained in this work would allow to fit the experimental spectra in order to validate the model indirectly. The results of this work will be published elsewhere.

4. Conclusions

AC current perturbation applied to the PEM fuel cell during EIS measurements causes oscillations of the mass injection velocity into the cathode channel through the channel/GDL interface. We report a model to rationalize the effect of these oscillations on the flow velocity and pressure in the channel. A transient model of laminar incompressible flow between parallel walls, one of which is permeable to mass suction/injection is developed. Following Berman's approach, two-dimensional transient Navier–Stokes equations and the continuity equation are reduced to a single equation for the streamwise flow velocity. Linearization and Fourier transformation lead to the ODE for the small perturbation amplitude of this velocity upon harmonic AC oscillations of the injection velocity.

The results show that a small perturbation of the injection velocity is translated into oscillations of the streamwise flow velocity and pressure gradient. At low frequencies, the transverse shape of the flow velocity oscillations amplitude resembles the Poiseuille parabola. However, at high frequencies, this shape flattens in the main body of the flow and two distinct peaks form at a distance $\sqrt{\nu/\omega}$ from the walls. The amplitude of the oscillations of streamwise flow velocity and pressure gradient increase linearly along the channel. Simple analytical formulas for incorporation of these effects into physics-based models for PEM fuel/electrolysis cell impedance are derived.

Declaration of competing interest

The authors declare that they have no known competing financial interests or personal relationships that could have appeared to influence the work reported in this paper.

Appendix. Comparison of the terms in Eq. (15)

Omitting the term with time derivative in Eq. (20), we get the equation which determines the steady-state solution of the problem with variable along $\tilde{x}$ injection velocity [2]:

$$(1+R)\tilde{w}\left(f'f'' - ff'''\right) - \left(\tilde{w}\tilde{w}' - (1+R)\tilde{w}''\right)ff' = \frac{1}{\mathrm{Re}}\left(2\tilde{w}'f'' + (1+R)f'''' + \tilde{w}'''f\right) \quad \text{(A.1)}$$

The numerical solution of Eq. (A.1) with the parameters from Table 1 allows us to calculate the ratio r of the terms in Eq. (15):

$$r(\tilde{x}) = \frac{(1+R)\|\partial f/\partial\tilde{x}\|_{\tilde{y}}}{\tilde{w}\|f\|_{\tilde{y}}} \quad \text{(A.2)}$$

where the subscript $\tilde{y}$ means that the norm is calculated along the $\tilde{y}$-coordinate. Calculations show that this ratio does not exceed 10^{-4}, meaning that the second term in Eq. (15) is negligible.

Data availability

No data was used for the research described in the article.

References

[1] G. Chao, Y. Shuili, S. Yufei, G. Zhengyang, Y. Wangzhen, R. Liumo, A review of ultrafiltration and forward osmosis: Application and modification, in: IOP Conference Series: Earth and Environmental Science, vol. 128, 2018, 012150, http://dx.doi.org/10.1088/1755-1315/128/1/012150.

[2] A. Kulikovsky, Laminar flow in a PEM fuel cell cathode channel, J. Electrochem. Soc. 170 (2023) 024510, http://dx.doi.org/10.1149/1945-7111/acba47.

[3] A.S. Berman, Laminar flow in channels with porous walls, J. Appl. Phys. 24 (1953) 1232–1235, http://dx.doi.org/10.1063/1.1721476.

[4] R.M. Terrill, P.W. Thomas, On laminar flow through a uniformly porous pipe, Appl. Sci. Res. 21 (1969) 37–67, http://dx.doi.org/10.1007/BF00411596.

[5] R.M. Terrill, Laminar flow in a porous tube, J. Fluids Eng. 105 (1983) 303–307, http://dx.doi.org/10.1115/1.3240992.

[6] A.A. Kosinski, F.P. Schmidt, E.N. Lightfoot, Velocity profiles in porous-walled ducts, Ind. Eng. Chem. Fundam. 9 (1970) 502–505, http://dx.doi.org/10.1021/i160035a033.

[7] J. Granger, J. Dodds, N. Midoux, Laminar flow in channels with porous walls, Chem. Eng. J. 42 (1989) 193–204, http://dx.doi.org/10.1016/0300-9467(89)80087-5.

[8] S.K. Karode, Laminar flow in channels with porous walls, revisited, J. Membr. Sci. 191 (2001) 237–241, http://dx.doi.org/10.1016/S0376-7388(01)00546-4.

[9] E.G. Richardson, E. Tyler, The transverse velocity gradient near the mouths of pipes in which an alternating or continuous flow of air is established, Proc. Phys. Soc. 42 (1929) 1–15, http://dx.doi.org/10.1088/0959-5309/42/1/302.

[10] T. Sexl, E.G. Über den von, Richardson entdeckten Annulareffekt, Z. Phys. 61 (1930) 349–362, http://dx.doi.org/10.1007/BF01340631.

[11] J. Harris, G. Peevt, W.L. Wilkinson, Velocity profiles in laminar oscillatory flow in tubes, J. Phys. E: Sci. Instrum. 2 (1969) 913–916, http://dx.doi.org/10.1088/0022-3735/2/11/301.

[12] T.E. Springer, T.A. Zawodzinski, M.S. Wilson, S. Gottesfeld, Characterization of polymer electrolyte fuel cells using AC impedance spectroscopy, J. Electrochem. Soc. 143 (1996) 587–599, http://dx.doi.org/10.1149/1.1836485.

[13] Y. Bultel, L. Genies, O. Antoine, P. Ozil, R. Durand, Modeling impedance diagrams of active layers in gas diffusion electrodes: Diffusion, ohmic drop effects and multistep reactions, J. Electroanal. Chem. 527 (2002) 143–155, http://dx.doi.org/10.1016/S0022-0728(02)00835-5.

[14] F. Jaouen, G. Lindbergh, Transient techniques for investigating mass–transport limitations in gas diffusion electrode, J. Electrochem. Soc. 150 (2003) A1699–A1710, http://dx.doi.org/10.1149/1.1624294.

[15] Q. Guo, R.E. White, A steady–state impedance model for a PEMFC cahode, J. Electrochem. Soc. 151 (2004) E133–E149.

[16] Y. Bultel, K. Wiezell, F. Jaouen, P. Ozil, G. Lindbergh, Investigation of mass transport in gas diffusion layer at the air cathode of a PEMFC, Electrochim. Acta 51 (2005) 474–488.

[17] D. Gerteisen, A. Hakenjos, J.O. Schumacher, AC impedance modelling study on porous electrodes of proton exchange membrane fuel cells using an agglomerate model, J. Power Sources 173 (2007) 346–356, http://dx.doi.org/10.1016/j.jpowsour.2007.04.071.

[18] A.A. Franco, P. Schott, C. Jallut, B. Maschke, A multi-scale dynamic mechanistic model for the transient analysis of PEFCs, Fuel Cells 7 (2007) 99–117.

[19] M. Cimenti, D. Bessarabov, M. Tam, J. Stumper, Investigation of proton transport in the catalyst layer of PEM fuel cells by electrochemical impedance spectroscopy, ECS Trans. 28 (23) (2010) 147–157, http://dx.doi.org/10.1149/1.3502346.

[20] I.A. Schneider, M.H. Bayer, S. von Dahlen, Locally resolved electrochemical impedance spectroscopy in channel and land areas of a differential polymer electrolyte fuel cell, J. Electrochem. Soc. 158 (2011) B343–B348.

[21] J. Mainka, G. Maranzana, A. Thomas, J. Dillet, S. Didierjean, O. Lottin, One-dimensional model of oxygen transport impedance accounting for convection perpendicular to the electrode, Fuel Cells 12 (2012) 848–861, http://dx.doi.org/10.1002/fuce.201100193.

[22] G. Maranzana, J. Mainka, O. Lottin, J. Dillet, A. Lamibrac, A. Thomas, S. Didierjean, A proton exchange membrane fuel cell impedance model taking into account convection along the air channel: On the bias between the low frequency limit of the impedance and the slope of the polarization curve, Electrochim. Acta 83 (2012) 13–27, http://dx.doi.org/10.1016/j.electacta.2012.07.065.

[23] J.R. Vang, S.J. Andreasen, S.K. Kaer, A transient fuel cell model to simulate HTPEM fuel cell impedance spectra, J. Fuel Cell Sci. Techn. 9 (2012) 021005–1–021005–9, http://dx.doi.org/10.1115/1.4005609.

[24] A.A. Kulikovsky, Exact low–current analytical solution for impedance of the cathode catalyst layer in a PEM fuel cell, Electrochim. Acta 147 (2014) 773–777, http://dx.doi.org/10.1016/j.electacta.2014.09.145.

[25] A.A. Kulikovsky, One–dimensional impedance of the cathode side of a PEM fuel cell: Exact analytical solution, J. Electrochem. Soc. 162 (2015) F217–F222, http://dx.doi.org/10.1149/2.0151503jes.

[26] T. Reshetenko, A. Kulikovsky, PEM fuel cell characterization by means of the physical model for impedance spectra, J. Electrochem. Soc. 162 (2015) F627–F633, http://dx.doi.org/10.1149/2.1141506jes.

[27] D. Gerteisen, Impact of inhomogeneous catalyst layer properties on impedance spectra of polymer electrolyte membrane fuel cells, J. Electrochem. Soc. 162 (2015) F1431–F1438, http://dx.doi.org/10.1149/2.0511514jes.

[28] A. Baricci, A. Casalegno, A simple analytical approach to simulate the electrochemical impedance response of flooded agglomerates in polymer fuel cells, Electrochim. Acta 157 (2015) 324–332, http://dx.doi.org/10.1016/j.electacta.2015.01.044.

[29] A.A. Kulikovsky, A simple physics–based equation for low–current impedance of a PEM fuel cell cathode, Electrochim. Acta 196 (2016) 231–235, http://dx.doi.org/10.1016/j.electacta.2016.02.150.

[30] T. Reshetenko, A. Kulikovsky, Impedance spectroscopy study of the PEM fuel cell cathode with nonuniform nafion loading, J. Electrochem. Soc. 164 (2017) E3016–E3021, http://dx.doi.org/10.1149/2.0041711jes.

[31] D. Vivona, A. Casalegno, A. Baricci, Validation of a pseudo 2D analytical model for high temperature PEM fuel cell impedance valid at typical operative conditions, Electrochim. Acta 310 (2019) 122–135, http://dx.doi.org/10.1016/j.electacta.2019.04.020.

[32] T. Reshetenko, A. Kulikovsky, Impedance spectroscopy characterization of oxygen transport in low– and high–pt loaded PEM fuel cells, J. Electrochem. Soc. 164 (2017) F1633–F1640, http://dx.doi.org/10.1149/2.1131714jes.

[33] A. Kosakian, M. Secanell, Estimating charge–transport properties of fuel–cell and electrolyzer catalyst layers via electrochemical impedance spectroscopy, Electrochim. Acta 367 (2021) 137521, http://dx.doi.org/10.1016/j.electacta.2020.137521.

[34] S. Cruz-Manzo, P. Greenwood, Analytical warburg impedance model for EIS analysis of the gas diffusion layer with oxygen depletion in the air channel of a PEMFC, J. Electrochem. Soc. 168 (2021) 074502, http://dx.doi.org/10.1149/1945-7111/ac1031.

[35] A.A. Kulikovsky, A model for local impedance of the cathode side of PEM fuel cell with segmented electrodes, J. Electrochem. Soc. 159 (2012) F294–F300, http://dx.doi.org/10.1149/2.066207jes.

[36] A.A. Kulikovsky, M. Eikerling, Analytical solutions for impedance of the cathode catalyst layer in PEM fuel cell: Layer parameters from impedance spectrum without fitting, J. Electroanal. Chem. 691 (2013) 13–17, http://dx.doi.org/10.1016/j.jelechem.2012.12.002.

[37] A.A. Kulikovsky, Analytical solutions for polarization curve and impedance of the cathode catalyst layer with fast oxygen transport in a PEM fuel cell, J. Electrochem. Soc. 161 (2014) E3171–E3179, http://dx.doi.org/10.1149/2.020408jes.

[38] I.A. Schneider, S.A. Freunberger, D. Kramer, A. Wokaun, G.G. Scherer, Oscillations in gas channels. part I. the forgotten player in impedance spectroscopy in PEFCs, J. Electrochem. Soc. 154 (2007) B383–B388, http://dx.doi.org/10.1149/1.2435706.

[39] I.A. Schneider, D. Kramer, A. Wokaun, G.G. Scherer, Oscillations in gas channels. ii. unraveling the characteristics of the low–frequency loop in air–fed PEFC impedance spectra, J. Electrochem. Soc. 154 (2007) B770–B3782, http://dx.doi.org/10.1149/1.2742291.

[40] A. Kulikovsky, O. Shamardina, A model for PEM fuel cell impedance: Oxygen flow in the channel triggers spatial and frequency oscillations of the local impedance, J. Electrochem. Soc. 162 (2015) F1068–F1077, http://dx.doi.org/10.1149/2.0911509jes.

[41] D. Grübl, J. Janek, W.G. Bessler, Electrochemical pressure impedance spectroscopy (epis) as diagnostic method for electrochemical cells with gaseous reactants: A model-based analysis, J. Electrochem. Soc. 163 (2016) A599–A610, http://dx.doi.org/10.1149/2.1041603jes.

[42] L. Schiffer, A.V. Shirsath, S. Raël, F. Lapicque, W.G. Bessler, Electrochemical pressure impedance spectroscopy for polymer electrolyte membrane fuel cells: A combined modeling and experimental analysis, J. Electrochem. Soc. 169 (2021) 034503, http://dx.doi.org/10.1149/1945-7111/ac55cd.

[43] A. Kulikovsky, Flow velocity oscillations in a PEM fuel cell cathode channel induced by harmonic pressure perturbations, J. Power Sources 558 (2023) 232544, http://dx.doi.org/10.1016/j.jpowsour.2022.232544.

[44] T. Berning, N. Djilali, A 3D, multiphase, multicomponent model of the cathode and anode of a PEM fuel cell, J. Electrochem. Soc. 150 (2003) A1598–A1607, http://dx.doi.org/10.1149/1.1621412.

[45] V. Gurau, T.A.Z. Jr., J.A.M. Jr., Two–phase transport in PEM fuel cell cathodes, J. Fuel Cell Sci. Techn. 5 (2008) 021009–1–021009–12, http://dx.doi.org/10.1115/1.2821597.

[46] P.C. Sui, S. Kumar, N. Djilali, Advanced computational tools for PEM fuel cell design. part 1. development and base case simulations, J. Power Sources 180 (2008) 410–422.

[47] H. Ly, E. Birgersson, M. Vynnycky, Asymptotically reduced model for a proton exchange membrane fuel cell stack: Automated model generation and verification, J. Electrochem. Soc. 157 (7) (2010) B982–B992.

[48] S. Zhang, S.B. Beale, U. Reimer, M. Andersson, W. Lehnert, Polymer electrolyte fuel cell modeling – A comparison of two models with different levels of complexity, Int. J. Hydrog. Energy 45 (2020) 19761–19777, http://dx.doi.org/10.1016/j.ijhydene.2020.05.060.

[49] L. Landau, E. Lifshitz, Fluid Mechanics, Pergamon Press, NY, 1987.

[50] T.V. Reshetenko, G. Bender, K. Bethune, R. Rocheleau, Systematic study of back pressure and anode stoichiometry effects on spatial PEMFC performance distribution, Electrochim. Acta 56 (2011) 8700–8710, http://dx.doi.org/10.1016/j.electacta.2011.07.058.

[51] E. Warburg, Über das Verhalten sogenannter unpolarisirbarer electroden gegen Wechselstrom, Ann. Phys. Und Chem. 67 (1899) 493–499, http://dx.doi.org/10.1002/andp.18993030302.